Chaos, Solitons and Fractals 186 (2024) 115244

Contents lists available at ScienceDirect

Chaos, Solitons and Fractals

journal homepage: www.elsevier.com/locate/chaos

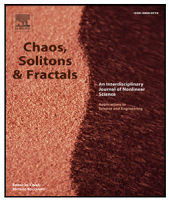

Characterization of Faraday patterns and spatiotemporal chaos in parametrically driven dissipative systems

L.I. Reyes [a], L.M. Pérez [b], L. Pedraja-Rejas [b], P. Díaz [c], J. Mendoza [d,e], J. Bragard [f,g], M.G. Clerc [h], D. Laroze [d,*]

[a] Laboratorio de Dinámica No-Lineal y Sistemas Complejos, Centro de Física, Instituto Venezolano de Investigaciones Científicas, IVIC, Apdo. 21827, Caracas 1020-A, Venezuela
[b] Departamento de Ingeniería Industrial y de Sistemas, Universidad de Tarapacá, Casilla 7D, Arica, Chile
[c] Departamento de Ciencias Físicas, Universidad de La Frontera, Casilla 54-D, Temuco, Chile
[d] Instituto de Alta Investigación, Universidad de Tarapacá, Casilla 7D, Arica, Chile
[e] Centro de Nanociencia y Nanotecnología, CEDENNA, Av. Libertador Bernardo O'Higgins 3363, Chile
[f] Departamento de Física y Matemática Aplicada, Universidad de Navarra, 31080, Pamplona, Spain
[g] Instituto de Ciencia de los Datos e Inteligencia Artificial, Universidad de Navarra, 31080, Pamplona, Spain
[h] Departamento de Física and Millennium Institute for Research in Optics, Facultad de Ciencias Físicas y Matemáticas, Universidad de Chile, Casilla 4873, Santiago, Chile

ARTICLE INFO

Keywords:
Faraday patterns
Spatiotemporal chaos
Lyapunov spectrum

ABSTRACT

In this work, we have studied numerically the dynamics of the parametrically driven damped nonlinear Schrödinger equation (PDDNLS). The PDDNLS is a universal model to describe parametrically driven systems. In particular, we have characterized stationary Faraday patterns, periodic, quasi-periodic, and spatiotemporal chaos as a function of the amplitude and the frequency of the parametric driving force. We have computed the Lyapunov spectra, the Fourier spectra, the amplitude norm, and the Kaplan–Yorke dimensions as valuable indicators for the identification of several dynamical regimes. We show that in the Faraday regime, close to the bifurcation of the trivial state, the pattern amplitude scales with power one-fourth (1/4) of the bifurcation parameter. Furthermore, we have found that the pattern wavelength decreases when the detuning parameter increases. In the case of the high dimensional spatiotemporal chaotic states, we have found that the Kaplan–Yorke dimension increases linearly with the length of the system, showing its extensive character in this dynamical regime. We have also found a transition from low to high dimensional chaos when the forcing amplitude is increased.

1. Introduction

Pattern formation and dissipative structures have been widely studied in science and technology [1]. Multiple physical and chemical systems exhibit a transition from a homogeneous state toward a patterned state. Many examples have been found in hydrodynamics, such as Taylor–Couette and Rayleigh–Bénard convection [2]; in solidification processes, nonlinear optics, oscillatory chemical reactions, biological systems, and granular media [3–6].

Spontaneous pattern formation has fascinated scientists for ages. These systems are examples of how a system out of thermodynamic equilibrium may organize itself into an ordered pattern. The great scientist Michael Faraday made a seminal contribution to the field of pattern formation [7]. He realized that a liquid layer vertically vibrated with a specific frequency and amplitude undergoes an instability to a patterned state. A critical driving force defines the onset of what is now called the Faraday instability [8]. After this first instability, the observed pattern consists of nonlinear surface waves (ripples) that organize themselves as stripes, squares, hexagons, and even quasi-crystals, depending on the system parameters and the excitation regimes [9]. Note that the Faraday instability is a parametric resonance where the created pattern oscillates at a frequency that is half of the excitation frequency.

Recently, one has observed a revival of interest in the study of the Faraday instability in the literature. Several studies have explored the Faraday instability in unexpected fields, for example, in Bose–Einstein condensates (BEC), where experimental and theoretical contributions have been proposed [10–12]. Another example is the non-linear optics domain, where parametric resonances are commonly observed in the

* Corresponding author.
E-mail address: dlarozen@academicos.uta.cl (D. Laroze).

https://doi.org/10.1016/j.chaos.2024.115244
Received 5 June 2024; Accepted 3 July 2024
Available online 27 July 2024

interactions between laser and matter [13,14]. In particular, due to their characteristics of very short length and time scales, the optical and BEC systems have allowed the researchers to explore dynamic regimes much further from the first Faraday instability that was conventionally observed in fluid systems. These studies have been pivotal in unveiling the secondary transitions that may lead to chaos and turbulence in those systems.

From a technological standpoint, the applications of the Faraday instability are becoming increasingly more relevant. One can cite, non-exhaustively, the crafting of hydrodynamic crystals at the fluid interface where the surface rigidity is modified thanks to the addition of surfactants [15]. Another technological application concerns using Faraday waves as frequency combs to perform spectroscopy in the acoustic range, with massive potential in biomedical imaging applications [16]. Finally, and complementary to the two previously mentioned applications, one can cite industrial ultrasonic atomization, which consists of the ejection of fine droplets from a liquid film formed on an ultrasonically vibrating surface [17]. The study of combined effects adds some interesting complexity to the fundamental Faraday wave instability problem. One can cite a few situations that have been studied recently. The non-homogeneity of the excitation unavoidable in many experimental systems leads to interesting localized patterns [18]. The competition of these localized structures has been investigated recently and has shown a variety of complex situations that result from this competition [19]. Finally, the interaction of the magnetic field and the forcing frequency in a Fermi–Fermi mixture has also led to new interesting dynamical situations in the context of the Faraday wave instability [20].

The classical techniques to deal with Faraday's pattern above the first instability threshold are well-known: these are based on the *amplitude equations* [21–24]. The amplitude equations describe the slow modulations in space and time of the periodic structure envelope. In the case of the Faraday instability, the description results in a parametrically driven and damped nonlinear Schrödinger equation (PDDNLS) [25]. This equation is the standard normal form for 2:1 parametric resonance, and has been deeply studied from theoretical and experimental point of view in optics, fluids or even in magnetism showing several dynamical behaviors [26–49]. Generalization and other applications of this equation can be found in Refs. [50–63].

Careful studies of the experimental characterization of Faraday's pattern have been reported in fluids [64]. Some experiments have reported the co-existence of two competing states in localized regions [65]. Faraday's instability has also been evidenced in multimode laser dynamics [66]. From the theory side, the competition between different patterns (squares, stripes, and hexagons) has been elucidated through asymptotic analysis of the amplitude equation near the threshold and also extensive numerical calculations [67,68]. A more involved experimental setup has investigated the possibility of Faraday's instability via parametric forcing with two commensurate frequencies [69], giving rise to superlattice and quasi-crystal patterns. These scaling laws associated with the spatiotemporal chaos in Faraday's surface waves were compared to scaling laws for turbulence and the differences were examined in [70]. The typical phenomenon of intermittency with a period of regular dynamics succeeding chaotic dynamics was also studied in great length in the context of Faraday's instability in [71–73] and compared with the classical theoretical predictions [74,75]. The connection between Faraday's waves on the surface of a vertically oscillated fluid layer and their relation with weak wave turbulence has been studied and shown to be generally disagreeing with each other [76]. Faraday's experiment with a fluid flowing down an inclined plane has been performed recently and compared satisfactorily with full numerical simulations in [77].

On the other hand, the characterization of spatiotemporal chaos has been studied in several contexts in recent years due to the access to improved computational power. Examples of complex spatiotemporal dynamics can be found in fluids, optics, coupled nonlinear oscillators, electric network devices, liquid crystals, chemical reactions, and cardiac dynamics, to mention a few. In the context of Faraday's instability, one can refer to the group of J. Gollub that performed a systematic experimental survey of both the primary patterns and the secondary instabilities of parametrically forced surface waves (Faraday waves) in the large system limit [78,79]. Universal scaling laws, a classical hallmark of chaos, have also been found in the Faraday instability in highly dissipative fluids [80,81]. Recently, a liquid crystal light valve experiment has led to the drawing of a complete bifurcation diagram of the observed complex spatiotemporal dynamics close to the spatial instability of waves [82].

The main characterization method used here is the computation of the Lyapunov exponents [83]. This paper aims to add numerical tools for the characterization of the secondary bifurcations of Faraday patterns in weakly dissipative parametrically driven systems described by PDDNLS equation. In particular, we will extensively compute the Lyapunov spectrum to characterize the level of the observed chaotic dynamics. We will also compute the associated Kaplan–Yorke dimension that indicates the dimension of the chaotic attractor [84]. The Fourier spectra are used to discriminate between periodic and quasi-periodic dynamics. In addition, the spatial average of the amplitude of the pattern is monitored in time as an additional dynamical indicator.

The manuscript is organized as follows: The model and some analytical results are presented in Section 2. Results of a systematic numerical exploration of the Faraday patterns and spatiotemporal chaos are given in Section 3. Finally, conclusions and future directions are drawn in Section 4.

2. The model and some analytical results

We consider an array of coupled nonlinear oscillators in the continuum limit under the action of dissipation as well as a parametrically driven forcing close to the parametric resonance. The system can be characterized by the parametrically driven dissipative nonlinear Schrödinger (PDDNLS) equation [26]:

$$\frac{\partial A}{\partial \tau} = -i\nu A - i|A|^2 A - i\frac{\partial^2 A}{\partial x^2} - \mu A + \gamma A^*, \tag{1}$$

where $A(\tau, x)$ is a complex-valued field; the asterisk stands for the complex conjugate of A; τ is a normalized time, and x is the normalized spatial coordinate. In Eq. (1), $\gamma > 0$ is the parametric-drive coefficient, ν measures the detuning of the drive, and $\mu > 0$ is the damping constant. Note that the nonlinearity coefficient is scaled to unity. Note also that the sign of the nonlinear term in Eq. (1) corresponds to the case of self-focusing onsite nonlinearity. Let us remind that we can also choose the scaling factor for A in Eq. (1) such that it allows fixing one of the equation parameters, which here will be the damping parameter, μ.

Let us mention some analytical results about the PDDNLS equation. First, Eq. (1) possesses the trivial solution $A = 0$ and two nontrivial homogeneous solutions, $A_{\pm,\pm} = \pm(1 \pm i\sqrt{(\gamma-\mu)/(\mu+\gamma)})x_0$ such that $x_0 \equiv \sqrt{(\gamma-\mu)(\phi-\nu)/2\gamma}$, with $\phi = \sqrt{\gamma^2-\mu^2}$. The two nontrivial solutions bifurcate from $A = 0$ at $\gamma^2 = \mu^2+\nu^2$. This latter relation defines the first Arnold's tongue commonly used in the γ versus ν diagrams. The study of the stability of trivial state was analyzed in Ref. [25], whereas for the nontrivial ones in Ref. [57]. Let us remark that in the special case $\mu = \gamma = 0$, Eq. (1) is reduced to the nonlinear Schrödinger equation, which is a time-reversible equation [85]. Let us comment that the model (1) exhibits also soliton-like solutions that have been studied extensively in [26,28], two-soliton states [30,31,47,48], or soliton-radiation [32], just to mention a few.

Examples of patterns exhibited in the solutions of Eq. (1) are shown in Fig. 1 for different dynamical scenarios. In Fig. 1, we have fixed the detuning and damping parameters and varied the forcing amplitude γ in the range $[0.301, 0.8]$. We observe in Fig. 1 transitions from stationary to regular dynamical states to further complex states, from simple Faraday waves to high-dimensional chaos. In the time window in Fig. 1, we can observe the collective spatiotemporal dynamics with the maximum resolution in time and space available. The numerical details for the integration of Eq. (1) are given in Section 3.

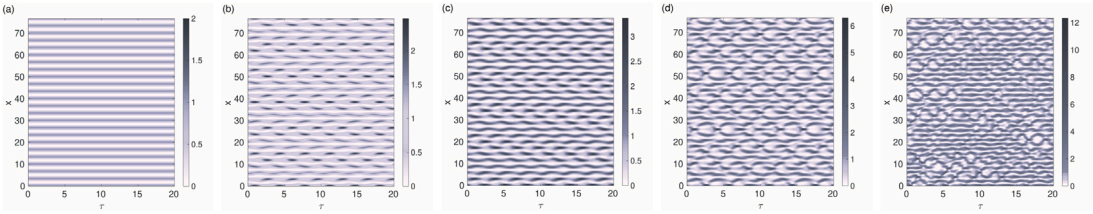

Fig. 1. Five panels showing the space–time dynamics of amplitude $|A|^2$ as color coded. Parameters in Eq. (1) are varied from regular to spatiotemporal chaotic dynamics (left to right panels). The chaotic level is quantified with the maximum Lyapunov exponent λ_{max}. From left to right: $\gamma = 0.390$ (Faraday waves, $\lambda_{max} = -0.0002$), $\gamma = 0.462$ (periodic state, $\lambda_{max} \approx 0$, up to the fourth decimal place), $\gamma = 0.534$ (quasi-periodic state, $\lambda_{max} \approx 0$, up to the fourth decimal place), $\gamma = 0.561$ (low dimensional chaos, $\lambda_{max} = 0.005$) and $\gamma = 0.687$ (high dimensional chaos, $\lambda_{max} = 0.117$). The other parameters, detuning $\nu = 0.4$ and damping $\mu = 0.3$ are held constant. For all the simulations, the transient time (not shown) was of 1.5×10^6 time units. (For interpretation of the references to color in this figure legend, the reader is referred to the web version of this article.)

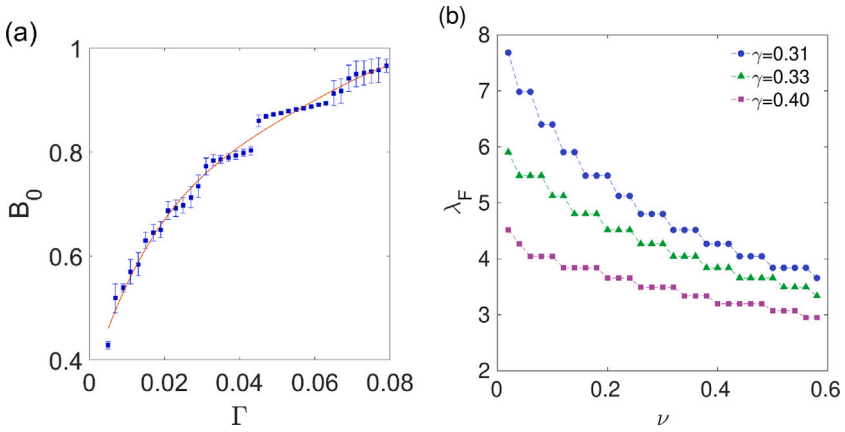

Fig. 2. (Color online) On the left panel (*a*), the squares indicate the pattern amplitudes extracted from the full simulation of Eq. (1) and the dashed line indicates the 1/4 predicted scaling law as a function of Γ for parameter $\nu = 0.3$ held constant. The right panel (*b*), displays the estimated Faraday wavelength λ_F (through the Fourier spectrum method; see text) in the case of stationary dynamics as a function of parameter $\nu > 0$. Squares correspond to $\gamma = 0.4$; triangles are for $\gamma = 0.33$, and circles are for $\gamma = 0.31$.

2.1. Instability of the trivial state: Faraday waves

To understand the mechanism of pattern formation in the model Eq. (1), let us briefly recall the results of the stability of the trivial solution $A = 0$ studied in Ref. [25]. Without the spatial term, the trivial state is stable outside of the Arnold's tongue. The spatial coupling, expressed by the Laplacian term in the PDDNLS Equation (dispersive term), modifies this scenario. The zero state exhibits a spatial instability at $\gamma = \mu$ for positive detuning, $\nu > 0$. This instability gives rise to the occurrence of a patterned state like the one shown in Fig. 1(a). Close to the bifurcation, the ansatz:

$$Re(A) = \left(B + \frac{1}{8\nu} B^3 e^{2ik_c Z}\right) e^{ik_c Z} + c.c. + \mathcal{O}(B^5)$$

$$Im(A) = -\frac{3}{2\gamma} B|B|^2 e^{ik_c Z} + c.c. + \mathcal{O}(B^5)$$

with $k_c \simeq \sqrt{\nu}$, results in an amplitude equation for the pattern amplitude B,

$$\frac{\partial B}{\partial \xi} = \Gamma B - \frac{9}{2\gamma}|B|^4 B - i\frac{\partial^2 B}{\partial Z^2}, \tag{2}$$

where $\Gamma = \gamma - \mu$ is the bifurcation parameter and $\xi = \Gamma\tau$ is the time scale. This equation has the form of a quintic Ginzburg–Landau equation for the complex amplitude B with real coefficients [25]. We remark that close to the bifurcation, the pattern amplitude B is constant and increases with Γ according to the power law, $|B_0| \sim \Gamma^{1/4}$. Let us remark that this law was experimentally observed on parametric mercury surface waves [86].

The pattern structure described by Eq. (2) not only exists and is stable for $\nu > 0$, for which it has been derived, but also for $\nu < 0$, if $\gamma^2 \geq \mu^2 + \nu^2$ (i.e. within the Arnold's tongue). By reducing γ (at negative ν), the pattern structure vanishes at the Arnold tongue border through a saddle–node bifurcation before reaching the $\gamma = \mu$ line.

The left panel of Fig. 2 compares the direct numerical simulations of Eq. (1) with the theoretical scaling prediction (as indicated by a dashed line). We observe an excellent agreement between the simulations and the theoretical predictions. The error bars in Fig. 2a depict the dispersion (plus and minus standard deviation) of the computed $|B_0|$ for a set of ten random different initials conditions per simulation point. We remark that we are focusing on the case of small forcing when $\Gamma \ll 1$. In addition, we can estimate the Faraday wavelength in the presence of stationary patterns. For this purpose, we first compute the square amplitude, $|A(\tau, x)|^2 = |A(x)|^2$, which is just a function of space, and then we compute its spatial Fourier transform:

$$\mathcal{F}(k) = \frac{1}{\sqrt{2\pi}} \int_0^L |A(x)|^2 \exp(-ikx)\, dx\,. \tag{3}$$

Later, we compute its power spectrum $|\mathcal{F}(k)|^2$, and from it, we extract its maximum peak located at k_F. The highest peak in the Fourier spectrum gives the approximate Faraday wavelength: $\lambda_F = 2\pi/k_F$. The right panel of Fig. 2 displays the Faraday wavelength λ_F as a function of the detuning parameter $\nu > 0$ for three selected values of γ. We observe from Fig. 2 that the Faraday wavelength decreases with ν but in a non-monotonous fashion. This stair-like decrease is due to the finite size effect in evaluating the dominant wavelength. Note that a similar wavelength decrease was recently recorded in an experiment of Faraday waves in a parametrically driven dissipative cold atom system [20]. Finally, it is interesting to note that closer to the bifurcation at $\gamma = \mu$, a wider range of values for λ_F can be reached.

In the previous situation, the dynamical regime leads to a stationary pattern. However, as we can observe from Fig. 1 if the parameter γ increases further, the pattern suffers multiple bifurcations and becomes chaotic. To the best of our knowledge, the full exploration of the spatiotemporal patterns of Eq. (1) has not yet been published. In the next section, we aim to numerically explore the regions of existence of the chaotic patterns and characterize their dynamics.

3. Spatiotemporal chaos

This section focuses on the spatiotemporal states observed after secondary bifurcations of the Faraday patterns take place. The first subsection describes the dynamical indicators that are used for their characterization. The second subsection describes the results of the numerical simulations through phase diagrams. The last subsection is devoted to quantifying the level of chaos in the spatiotemporal states.

Let us first briefly comment on the numerical integration scheme. To solve numerically the amplitude equation, Eq. (1), we use a classical fourth-order Runge–Kutta (RK) scheme for the time evolution and a second-order central finite difference method to discretize space. The system length L is discretized with $N = 512$ lattice points separated by $\Delta x = 0.15$, which implies a system size of $L = N\Delta x \approx 77$. At the edge of the spatial domain, we impose Neumann boundary conditions. Temporal discretization is set to $\Delta t = 0.001$ to ensure stability and high accuracy of the time integration scheme. All the simulations have been performed with a fixed damping coefficient value, $\mu = 0.3$. The initial conditions for the amplitude follow the homogeneous stationary pattern obtained for parameters $\nu = 0.6$ and $\gamma = 0.35$. The algorithm schemes were implemented in the C programming language [87], and the Fourier libraries needed for the subsequent analysis were borrowed from the open-access GSL libraries [88]. We have also checked the simulations using a Python code, with the library *Numpy* [89]. Let us emphasize that the spatial grid resolution Δx was chosen such that the Faraday wavelength λ_F (see Fig. 2) was notably larger than Δx for the parameters that we have explored in this work. Finally, let us remark that for all the simulations, we discard a transient time of 1.5×10^6 time units before measuring any of the dynamical indicators. This elapsed transient ensures that we are not measuring transitory regimes but stationary states. We have checked several values of the transient time to ensure that the considered states have converged into a steady one.

3.1. Dynamical indicators

Presumably, the most relevant indicators for the characterization of the dynamics are given by the Lyapunov exponents [90,91]. The set of the Lyapunov exponents constitutes the Lyapunov spectrum. In principle, the Lyapunov spectrum can be continuous in the case of spatiotemporal dynamics. However, due to the discretization of the numerical scheme, we only get a discrete representation of the Lyapunov spectrum. Practically, it is obtained by computing the time evolution of the perturbation vectors δA_k of the linearized system according to:

$$\frac{\partial \delta A_k}{\partial \tau} = \bar{\mathbf{J}} \cdot \delta A_k, \tag{4}$$

where $\bar{\mathbf{J}}$ is the Jacobian matrix of Eq. (1) evaluated along the dynamical trajectory of Eq. (1). The vectors δA_k have N components and $k = 1, 2, \ldots, N_{pert}$, with $N_{pert} \leq N$. With the integration of Eqs. (4) over a time interval t_s, one can compute *instantaneous* Lyapunov exponents as:

$$\widetilde{\Lambda}_k = \frac{1}{t_s} \ln \frac{\|\delta A_k\|_{t_s}}{\|\delta A_k\|_0} \tag{5}$$

where $\|\delta A_k\|_0$ is the vector norm at the beginning of the time integration interval. After renormalization of the perturbation vectors δA_k, the process is repeated N_s times to compute an estimate of the finite time Lyapunov exponent:

$$\Lambda_k = \frac{1}{N_s} \sum_{i=1}^{N_s} \widetilde{\Lambda}_k, \tag{6}$$

where N_s denotes the number of renormalizations performed. Note that we also evaluated the standard error of each of the Lyapunov exponents by also computing the second moment of $\widetilde{\Lambda}_k$. The limit $N_s \to \infty$ yields the steady state Lyapunov exponent.

In the numerical scheme, the renormalization actually consists in an ortho-normalization of the different perturbation vectors δA_k through the Gram–Schmidt algorithm. This procedure is repeated every t_s time unit [90]. The set of Lyapunov exponents $k = 1, 2, \ldots, N_{pert}$ forms the Lyapunov spectrum associated with the Eq. (1). From a practical point of view, here we have followed the numerical approach given in Ref. [91]. Let us remark that the Lyapunov exponents $\{\lambda_i\}$ have been used in the characterization of many dynamical systems [92–111].

In the second step, once the Lyapunov spectrum has been computed and ordered from largest to smallest, we compute the Kaplan–Yorke dimension D_{KY} following the formula [84]:

$$D_{KY} = p + \frac{1}{|\lambda_{p+1}|} \sum_{i=1}^{p} \lambda_i, \tag{7}$$

where p is the largest integer such that the sum of the first p Lyapunov exponents is non-negative. The Kaplan–Yorke dimension D_{KY} is conjectured to give the dimension of the chaotic attractor. For regular states, one gets that $D_{KY} = 0$, whereas $D_{KY} > 0$ means a chaotic state. We can also infer that when D_{KY} is small with respect to N, one has a dynamical state of low-dimensional chaos.

From the numerical point of view, we have set $N_{pert} = 128$ perturbation vectors δA_k. That means we must solve N_{pert} copies of the variational Eq. (4). We have set $t_s = \Delta t$, which means that we reorthonormalize the perturbation vectors δA_k at each time step [91]. We have checked that $N_{pert} = 128$ perturbation vectors are sufficient to ensure an accurate estimate of the Kaplan–Yorke dimension in the parameter space $\{\gamma - \nu\}$ considered here. The number of perturbation vectors N_{pert} drastically affects the computation time because each new perturbation vector δA_k implies the solution of an additional variational Eq. (4). Hence, the correct election of N_{pert} is essential to optimize the parameter space exploration.

Let us remark that transients are also important in evaluating the Lyapunov spectrum. Here, we solve Eq. (1) for a transient time of 1.5×10^6, and then we start to solve Eq. (1) and Eqs. (4) for another 3×10^4 time units. After this second transient time, we use only the last 5×10^3 time units to compute the average Lyapunov spectrum Λ_k. The Kaplan–Yorke dimension D_{KY} is evaluated once the Lyapunov spectrum Λ_k is obtained.

To validate our Lyapunov spectrum code, we have reproduced several results regarding the Kaplan–Yorke dimension that are available in the literature. In particular, we have successfully reproduced D_{KY} for the Lorenz-96 model [91] and the Lugiato–Lefever model [112–114].

Another relevant quantity to characterize different dynamical behaviors is the total norm of the amplitude:

$$Q_\tau = \frac{1}{L} \int_0^L |A(\tau, x)|^2 \, dx. \tag{8}$$

Note that Q_τ is a dynamical invariant for the NLS equation (when the damping and parametric force are vanishing), and it is time-independent when the dynamical state is steady. On the contrary, it is a function of time for non-stationary states. In the latter case, we can compute the temporal Fourier spectrum of Q_τ, $S(f) = |\mathcal{F}(f)|^2$, as a function of the time–frequency f. The temporal Fourier transform of the function Q_τ is evaluated through:

$$\mathcal{F}_Q(f) = \frac{1}{\sqrt{2\pi}} \int_0^{\tau_{\max}} Q_\tau \exp(-if\tau) \, d\tau. \tag{9}$$

A general result is that $S(f)$ features a quasi-discrete spectrum with a set of narrow peaks that indicates regular solutions, which exhibit (quasi-) periodic evolution in time. On the other hand, the spectrum is expected to be continuous if the underlying time-dependent solution is chaotic. Practically, the Fourier transform was numerically computed using the open GSL library [88].

3.2. Phase diagrams of the dynamical states

In this section, we analyze the results provided by the dynamical indicators. The maximum Lyapunov exponent and dynamical states in the $\gamma - \nu$ parameter space are displayed in Fig. 3.

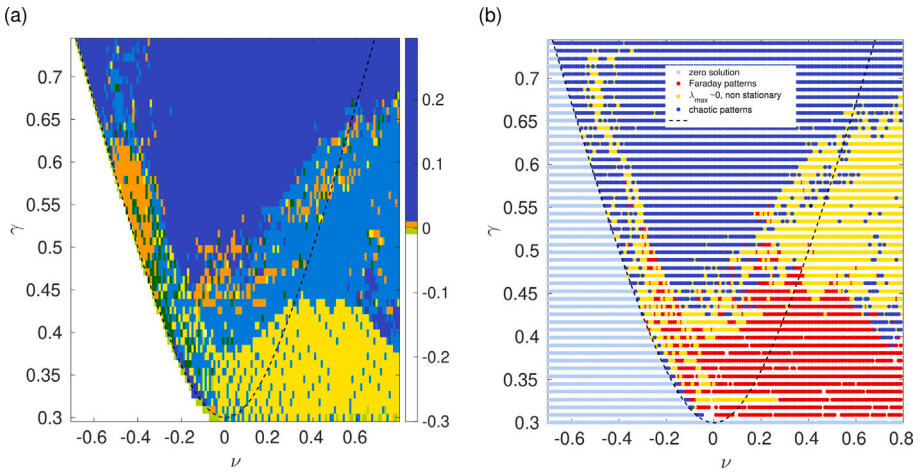

Fig. 3. Maximum Lyapunov exponent (left) and dynamical states (right, see text) in $\gamma - \nu$ parameter space for the PDDNLS equation. On the left, the colors indicate the following ranges: white, less than −0.01; light green, −0.01 to −0.001; yellow, −0.001 to −0.0001; light blue, −0.0001 to +0.0001; green, +0.0001 to 0.001; orange, 0.001 to 0.01; blue, greater than 0.01. On the right panel, the red dots correspond to Faraday waves. Yellow dots correspond to non-stationary states with small Lyapunov exponent (see text), while blue dots correspond to chaotic patterns. Dashed lines in both figures indicate the Arnold's tongue limits. (For interpretation of the references to color in this figure legend, the reader is referred to the web version of this article.)

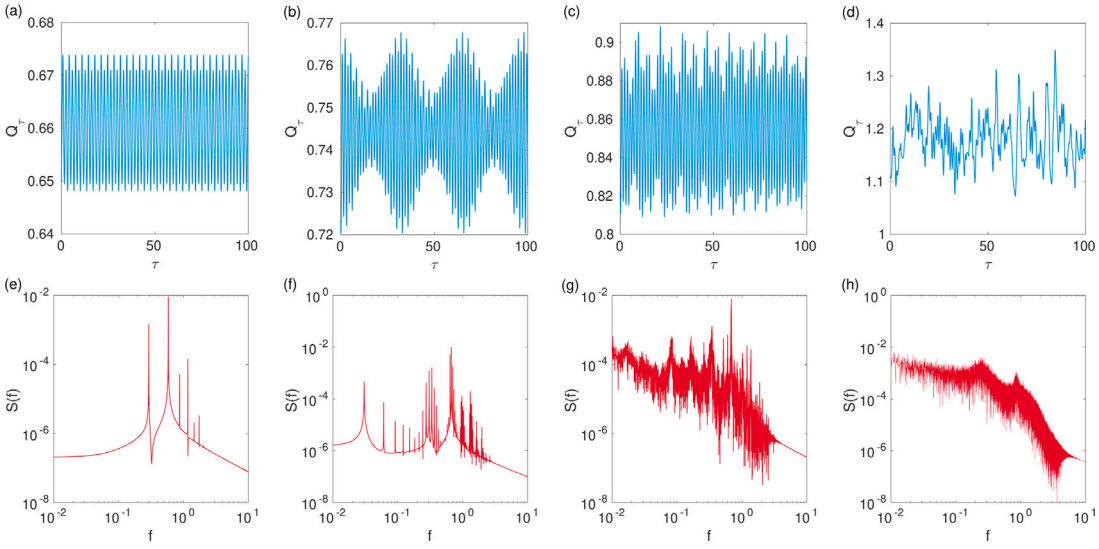

Fig. 4. (Color online) Upper panels show the time evolutions of the norm Q (Eq. (8)) and the lower panels their corresponding Fourier power spectra $S(f)$ (see text for details) for four characteristic dynamical scenarios. (a) and (e): $\gamma = 0.462$. (b) and (f) : $\gamma = 0.534$. (c) and (g) : $\gamma = 0.561$. (d) and (h) : $\gamma = 0.687$. The detuning parameter is hold to $\nu = 0.4$ in all cases. See also the corresponding patterns given in Fig. 1.

In Fig. 3, we observe that the left border given by the Arnold's tongue coincides with the limit between space–time chaos and zero solution (fixed point solution corresponding to $A = 0$). On the contrary, the right border of the Arnold's tongue does not discriminate dynamic states. Depending on the parameters $\gamma - \nu$, the dynamical state settles to a regular Faraday wave pattern, quasi-periodic pattern, or space–time chaos, as illustrated in Fig. 1.

Due to the numerical precision of the calculations of the Lyapunov exponents, we will consider as vanishing a Lyapunov exponent that satisfies the following condition of $|\lambda| < 10^{-4}$. Note that longer and more costly simulations would lower this limit for considering vanishing exponents.

Of particular relevance is the maximum Lyapunov exponent Λ_{max} as shown in Fig. 3(a). This dynamical indicator quantifies how fast the distance between two initially close trajectories δA of the vector field A either vanishes exponentially ($\Lambda_{max} < 0$) or diverges ($\Lambda_{max} > 0$). Fig. 3(b) displays that the parameters $\gamma - \nu$ selects the dynamical state of the system governed by Eq. (1).

3.3. Spatiotemporal chaos

In this last subsection, let us concentrate on the analysis of the spatiotemporal chaos exhibited in Eq. (1).

Fig. 4 displays four different typical dynamical behaviors exhibited by the PDDNLS Eq. (1) as detected by the norm of Q_τ and their corresponding temporal Fourier spectra. Note that the spatiotemporal patterns associated with the specific parameter values used in Fig. 4 are displayed in Fig. 1. They correspond with increasing values of the parameter γ of periodic, quasi-periodic, low dimensional, and high dimensional chaos.

The Lyapunov spectra and their cumulative sums $\sum \lambda_i$ are displayed in Fig. 5. From the calculations of the Lyapunov spectra, one can evaluate the Kaplan–Yorke dimension by using Eq. (7). In panel (b) of Fig. 5, we checked the expected extensivity [91] of D_{KY} with respect to the dimension of the system (spatial extension indicated by N the number of grid points). Note that the inset of panel (b) of Fig. 5 shows the collapse of the Lyapunov spectrum to a single curve within numerical fluctuations when the exponents are plotted against the spatial scaled

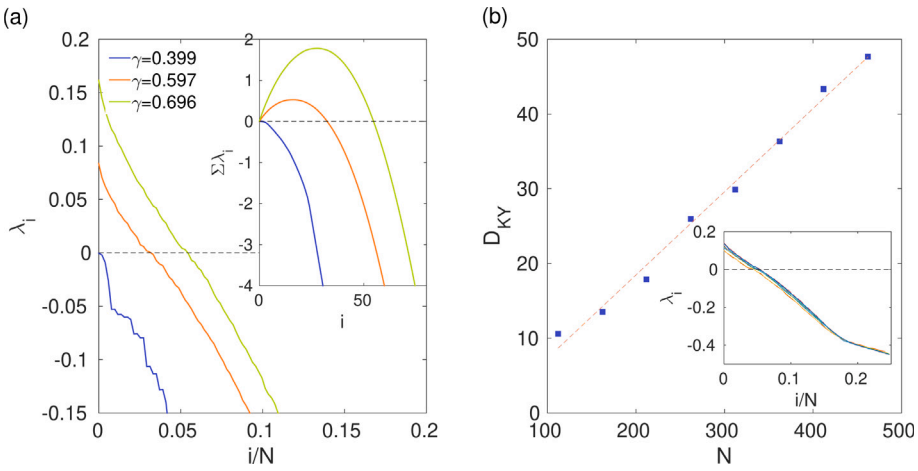

Fig. 5. (a) The Lyapunov spectra for three representative values of the parameter γ ($\gamma = 0.399$ blue curve; $\gamma = 0.597$ orange curve; $\gamma = 0.696$ green curve), with $\nu = 0.3$ held constant. The inset in panel (a) shows the calculated cumulative sum of the ordered exponents $\sum \lambda_i$. The crossing with $\sum \lambda_i = 0$ gives the Kaplan–Yorke dimension D_{KY}. (b) Extensivity of D_{KY}, as a function of the system size (here indicated with the number of grid points N). The scaling of D_{KY} with N is obtained for parameters $\gamma = 0.7$ and $\nu = 0.2$. This linear scaling is expected in chaotic dynamical scenarios [91]. The inset in panel (a) shows the collapse, within numerical fluctuations, of the Lyapunov spectrum when we plot the Lyapunov exponents λ_i versus the space scaled index i/N. (For interpretation of the references to color in this figure legend, the reader is referred to the web version of this article.)

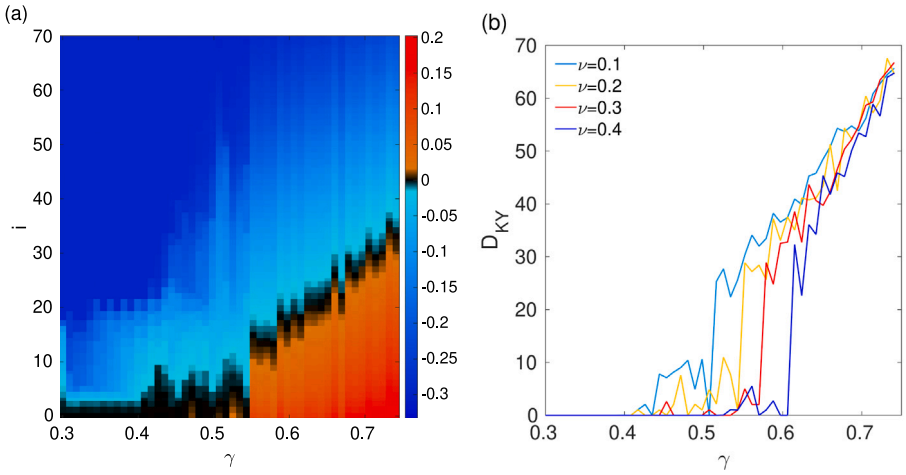

Fig. 6. A transition to spatio-temporal chaotic dynamics of increased dimensionality in parameter space. On the left it is shown the Lyapunov spectrum in color bar code as a function of oscillator's number and forcing parameter γ at $\nu = 0.2$. On the right the Kaplan–Yorke dimension D_{KY} as a function of γ for $\nu = 0.1$, $\nu = 0.2$, $\nu = 0.3$ and $\nu = 0.4$. (For interpretation of the references to color in this figure legend, the reader is referred to the web version of this article.)

index i/N. From a numerical point of view, we can discern between a Faraday's wave regime and a high-dimensional chaotic regime using this dynamical indicator.

Let us discuss the distinction between low- and high-dimensional chaos. In the left panel of Fig. 6, the color code indicates the Lyapunov exponent values as a function of the forcing parameter γ and the spatial index i for fixed values of $\nu = 0.2$ and $N = 512$ lattice points. The region without chaos corresponding to the Faraday waves regime is clearly shown between $\gamma = 0.3$ and $\gamma = 0.4$ (approximately). An increase of the parameter γ in the range between about 0.4 and 0.55 shows a region of low-dimensional chaos. Finally, if γ is larger than 0.55, one observes that the number of positive Lyapunov exponents increases linearly with γ, showing a region of extensive spatiotemporal chaos.

In the right panel of Fig. 6, the computed Kaplan–Yorke dimension D_{KY}, Eq. (7), is displayed as a function of the parameter γ for several values of the detuning parameter ν. It is especially interesting to note that the approximations of the partial derivatives $\partial D_{KY}/\partial\gamma$ and $\partial D_{KY}/\partial\nu$ provide good indicators for identifying corresponding dynamical states. Indeed, the Faraday waves regime (here for small γ between 0.3 and 0.4) and the high dimensional chaotic regime (values of $\gamma > 0.6$) share the condition that both partial derivatives are constant, as it can be shown in the right panel of Fig. 6. For intermediate values of γ, the system is in the low dimensional chaotic regime, and $\partial D_{KY}/\partial\gamma$ fluctuates considerably, and large variations of D_{KY} are observed if the detuning parameter ν is varied.

4. Conclusions

In this paper, we have studied the dynamics associated with the PDDNLS equation numerically. We have shown that if the forcing amplitude is small, we observe the classical Faraday pattern. Increasing the forcing amplitude allows periodic, quasi-periodic, and chaotic dynamics to be observed. The dynamics were studied through several indicators, i.e., Lyapunov and Fourier spectra, Kaplan–Yorke dimension, and averaged amplitude norm. Using the information provided by these indicators, the phase diagrams of these dynamical states were built as a function of the amplitude and detuning of the parametrical forcing. Furthermore, the system size plays an important role in discriminating between low and high-dimensional chaos. In the latter case, the Kaplan–Yorke dimension scales linearly with the system size, ultimately proving its extensive property.

The present study's natural extensions will consider two-dimensional settings for the PDDNLS equation. In this case, one expects to encounter competing stationary patterns with spatiotemporal chaos that will further increase the complexity of the phase diagrams of the dynamic states.

CRediT authorship contribution statement

L.I. Reyes: Data curation, Investigation, Methodology, Software, Visualization, Writing – original draft. **L.M. Pérez:** Formal analysis, Investigation, Resources, Validation, Writing – review & editing. **L. Pedraja-Rejas:** Data curation, Software, Visualization. **P. Díaz:** Formal analysis, Investigation, Software, Visualization. **J. Mendoza:** Data curation, Software, Visualization. **J. Bragard:** Formal analysis, Investigation, Validation, Writing – review & editing. **M.G. Clerc:** Conceptualization, Formal analysis, Methodology, Supervision, Writing – review & editing. **D. Laroze:** Conceptualization, Funding acquisition, Investigation, Supervision, Validation, Writing – original draft, Project administration.

Declaration of competing interest

The authors declare that they have no competing interests.

Data availability

Data will be made available on request.

Acknowledgments

LMP acknowledges partial financial support from ANID through Convocatoria Nacional Subvención a Instalación en la Academia Convocatoria Año 2021, Grant SA77210040. LMP, PD and DL acknowledge partial financial support from FONDECYT 1231020. JB acknowledges partial financial support from MINECO (Spain) research project with reference: PID2020-116927RB-C22. MGC acknowledges partial financial support from ANID- Millennium Science Initiative Program-ICN17-012 (MIRO). MGC and DL acknowledge partial financial support from FONDECYT 1210353. DL acknowledges partial financial support from Centers of Excellence with BASAL/ANID financing, AFB220001, CEDENNA. Besides, DL acknowledges the hospitality of *Instituto de Ciencia de los Datos e Inteligencia Artificial* (Spain) where part of manuscript was written.

References

[1] Cross MC, Hohenberg PC. Pattern formation outside of equilibrium. Rev Modern Phys 1993;65:851.
[2] Norm C, Pomeau Y, Velarde MG. Convective instability: a physicist's approach. Rev Modern Phys 1977;49:581.
[3] Turing AM. The chemical basis of morphogenesis. Philos Trans R Soc Lond B 1952;237:37.
[4] Gollub JP, Langer JS. Pattern formation in nonequilibrium physics. Rev Mod Phys 1999;71:396.
[5] Aranson IS, Tsimring LS. Patterns and collective behavior in granular media: Theoretical concepts. Rev Modern Phys 2006;78:641.
[6] Aranson IS, Kramer L. The world of the complex Ginzburg–Landau equation. Rev Modern Phys 2002;74:99.
[7] Faraday M. On a peculiar class of acoustical figures; and on certain forms assumed by groups of particles upon vibrating elastic surfaces. Phil Trans R Soc 1831;121:299.
[8] Rajchenbach J, Clamond D. Faraday waves: their dispersion relation, nature of bifurcation and wavenumber selection revisited. J Fluid Mech 2015;777:382.
[9] Christiansen B, Alstrom P, Levinsen MT. Ordered capillary-wave states: quasicrystals, hexagons, and radial waves. Phys Rev Lett 1992;68:2157.
[10] Engels P, Atherton C, Hoefer MA. Observation of Faraday waves in a Bose–Einstein condensate. Phys Rev Lett 2007;98:5301.
[11] Nicolin AI, Carretero-González R, Kevrekidis PG. Faraday waves in Bose–Einstein condensates. Phys Rev A 2007;76:3609.
[12] Nguyen J, Tsatsos M, Luo D, Lode A, Telles G, Bagnato V, Hulet R. Parametric excitation of a Bose–Einstein condensate: From Faraday waves to granulation. Phys Rev X 2019;9:1052.
[13] Staliunas K, Hang C, Konotop V. Parametric patterns in optical fiber ring nonlinear resonators. Phys Rev A 2013;88:3846.
[14] García-Ripoll J, Pérez-García VM, Torres P. Extended parametric resonances in nonlinear Schrödinger systems. Phys Rev Lett 1999;83:1715.
[15] Kharbedia M, Caselli N, Herráez-Aguilar D, López-Menéndez H, Enciso E, Santiago J, et al. Moulding hydrodynamic 2D-crystals upon parametric Faraday waves in shear-functionalized water surfaces. Nat Comm 2021;12:1130.
[16] Maksymov I, Nguyen B, Pototsky A, Suslov S. Phononic, brillouin light scattering and Faraday wave-based frequency combs: Physical foundations and applications. Sensors 2022;22:3921.
[17] Yuan S, Zhang Y, Gao Y. Faraday instability of a liquid layer in ultrasonic atomization. Phys Rev Fluids 2022;7:3902.
[18] Urra H, Marín J, Páez-Silva M, Taki M, Coulibaly S, Gordillo L, et al. Localized Faraday patterns under heterogeneous parametric excitation. Phys Rev E 2019;99:033115.
[19] Marín JF, Riveros Avila R, Coulibaly S, Taki M, García-Ñustes MA. Drift instabilities in localised faraday patterns. 2021, arXiv:2112.03866v1.
[20] Díaz P, Pérez LM, Reyes LI, Laroze D, Bragard J. Taming Faraday waves in binary fermionic clouds: The effect of Zeeman interaction. Chaos Solitons Fractals 2021;153:111416.
[21] Fauve S. Pattern forming instabilities. In: Godrèche C, Manneville P, editors. Hydrodynamics and nonlinear instabilities. Cambridge University Press; 1998, p. 387–491.
[22] Pismen LM. Patterns and interfaces in dissipative dynamics. Berlin: Springer; 2006.
[23] Manneville P. Instabilities, chaos and turbulence. London: Imperial college Press; 2004.
[24] Walgraef D. Spatio-temporal pattern formation: with examples from physics, chemistry, and materials science. Springer Science & Business Media; 2012.
[25] Coullet P, Frisch T, Sonnino G. Dispersion-induced patterns. Phys Rev E 1994;49:2087.
[26] Barashenkov IV, Bogdan MM, Korobov VI. Stability diagram of the phase-locked solitons in the parametrically driven, damped nonlinear Schrödinger equation. Europhys Lett 1991;15:113.
[27] Barashenkov IV, Zemlyanaya EV. Stable complexes of parametrically driven, damped nonlinear Schrödinger solitons. Phys Rev Lett 1999;83:2568.
[28] Barashenkov IV, Zemlyanaya EV, van Heerden TC. Time-periodic solitons in a damped-driven nonlinear Schrödinger equation. Phys Rev E 2011;83:056609.
[29] Quispe-Flores L, Urzagasti D. Hamiltonian approach to the soliton-soliton interaction and for a classical solitonic gas. Phys Lett A 2022;429:127967.
[30] Barashenkov IV, Zemlyanaya EV. Soliton complexity in the damped-driven nonlinear Schrödinger equation: Stationary to periodic to quasiperiodic complexes. Phys Rev E 2011;83:056610.
[31] Urzagasti D, Laroze D, Clerc MG, Coulibaly S, Pleiner H. Two-soliton precession state in a parametrically driven magnetic wire. J Appl Phys 2012;111:07D111.
[32] Shchesnovich VS, Barashenkov IV. Soliton-radiation coupling in the parametrically driven, damped nonlinear Schrödinger equation. Phys D 2002;164:83.
[33] Alexeeva NV, Barashenkov IV, Tsironis GP. Impurity-induced stabilization of solitons in arrays of parametrically driven nonlinear oscillators. Phys Rev Lett 2000;84:3053.
[34] Barashenkov IV, Alexeeva NV, Zemlyanaya EV. Two- and three-dimensional oscillons in nonlinear Faraday resonance. Phys Rev Lett 2002;89:104101.
[35] Zemlyanaya EV, Alexeeva NV. Oscillating solitons of the driven, damped nonlinear Schrödinger equation. Theoret Math Phys 2009;159:870.
[36] Urzagasti D, Laroze D, Clerc MG, Pleiner H. Breather soliton solutions in a parametrically driven magnetic wire. Europhys Lett 2013;104:40001.
[37] Urzagasti D, Aramayo A, Laroze D. Soliton-antisoliton interaction in a parametrically driven easy-plane magnetic wire. Phys Lett A 2014;378:2614.
[38] Gordillo L, García-Ñustes MA. Phys Rev Lett 2014;112:164101.
[39] Leon AO, Laroze D, Clerc MG, Cabanas AM. Alternating superlattice textures in driven nanomagnets. Commun Nonlinear Sci Numer Simul 2017;44:404.
[40] Cabanas AM, Clerc MG, Laroze D, Leon AO. Chaotic patterns and localized states in spin valves. J Magn Magn Mater 2019;476:589.
[41] Cabanas AM, Vélez JA, Pérez LM, Díaz P, Clerc MG, Laroze D, et al. Dissipative structures in a parametrically driven dissipative lattice: Chimera, localized disorder, continuous-wave, and staggered states. Chaos Solitons Fractals 2021;146:110880.
[42] Cabanas AM, Rivas R, Pérez LM, Vélez JA, Díaz P, Clerc MG, et al. A quasi-periodic route to chaos in a parametrically driven nonlinear medium. Chaos Solitons Fractals 2021;151:111089.
[43] Bondila M, Barashenkov IV, Bogdan MM. Topography of attractors of the parametrically driven nonlinear Schrödinger equation. Phys D 1995;87:314.
[44] Alexeeva NV, Barashenkov IV, Pelinovsky DE. Dynamics of the parametrically driven NLS solitons beyond the onset of the oscillatory instability. Nonlinearity 1999;12:103.
[45] Barashenkov IV, Woodford SR. Interactions of parametrically driven dark solitons. II. Néel-Bloch interactions. Phys Rev E 2007;75:026605.

[46] Barashenkov IV, Zemlyanaya EV, Bär M. Traveling solitons in the parametrically driven nonlinear Schrödinger equation. Phys Rev E 2001;64:016603.
[47] Wang X. Nature of the parametrically excited bound soliton state. Phys Rev E 1998;58:7899.
[48] Wang X, Wei R. Oscillatory patterns composed of the parametrically excited surface-wave solitons. Phys Rev E 1998;57:2405.
[49] García-Ñustes MA, Humire FR, Leon AO. Self-organization in the one-dimensional Landau–Lifshitz–Gilbert–Slonczewski equation with non-uniform anisotropy fields. Commun Nonlinear Sci Numer Simul 2021;96:105674.
[50] Barashenkov IV, Cross S, Malomed BA. Multistable pulselike solutions in a parametrically driven Ginzburg–Landau equation. Phys Rev E 2003;68:056605.
[51] Clerc MG, Coulibaly S, Laroze D. Localized states beyond the asymptotic parametrically driven amplitude equation. Phys Rev E 2008;77:056209.
[52] Kenig E, Malomed BA, Cross MC, Lifshitz R. Intrinsic localized modes in parametrically driven arrays of nonlinear resonators. Phys Rev E 2009;80:046202.
[53] Burke J, Yochelis A, Knobloch E. Classification of spatially localized oscillations in periodically forced dissipative systems. SIAM J Appl Dyn Syst 2008;7:651.
[54] Clerc MG, Coulibaly S, Laroze D. Parametrically driven instability in quasi-reversal systems. Int J Bifurcation Chaos 2009;19:3525.
[55] Clerc MG, Coulibaly S, Laroze D. Nonvariational Ising-Bloch transition in parametrically driven systems. Int J Bifurcation Chaos 2009;19:2717.
[56] Clerc MG, Coulibaly S, Laroze D. Interaction law of 2D localized precession states. Europhys Lett 2010;90:38005.
[57] Clerc MG, Coulibaly S, Laroze D. Localized states and non-variational Ising-Bloch transition of a parametrically driven easy-plane ferromagnetic wire. Phys D 2010;239:722010.
[58] Ma YP, Burke J, Knobloch E. Defect-mediated snaking: A new growth mechanism for localized structures. Phys D 2010;239:1867.
[59] Clerc MG, Coulibaly S, Laroze D. Localized waves in a parametrically driven magnetic nanowire. Europhys Lett 2012;97:30006.
[60] Urzagasti D, Laroze D, Pleiner H. Localized chaotic patterns in weakly dissipative systems. Eur Phys J ST 2014;223:141.
[61] Urzagasti D, Laroze D, Pleiner H. Two-dimensional localized chaotic patterns in parametrically driven systems. Phys Rev E 2017;95:052216.
[62] Clerc MG, Coulibaly S, Laroze D, León AO, Nuñez ÁS. Alternating spin-polarized current induces parametric resonance in spin valves. Phys Rev B 2015;91:224426.
[63] Díaz P, Molinares H, Pérez LM, Laroze D, Bragard J, Malomed BA. Stable semivortex gap solitons in a spin–orbit-coupled Fermi gas. Chaos Solitons Fractals 2024;179:114456.
[64] Wernet A, Wagner C, Papathanassiou D, Müller HW, Knorr K. Amplitude measurements of Faraday waves. Phys Rev E 2001;63:036305.
[65] Kudrolli A, Gollub JP. Localized spatiotemporal chaos in surface waves. Phys Rev E 1996;54. R1052(R).
[66] Ch Szwaj, Bielawski S, Derozier D, Erneux Th. Faraday instability in a multimode laser. Phys Rev Lett 1998;80:3968.
[67] Chen P, Viñals J. Amplitude equation and pattern selection in Faraday waves. Phys Rev E 1999;60:559.
[68] Zhang W, Viñals J. Numerical study of pattern formation in weakly damped parametric surface waves. Phys D 1998;116:225.
[69] Arbell H, Fineberg J. Pattern formation in two-frequency forced parametric waves. Phys Rev E 2002;65:036224.
[70] Bosch E, van de Water W. Spatiotemporal chaos in the Faraday effect. Appl Sci Res 1993;51:15.
[71] Feldmann D, Morón D, Avila M. Spatiotemporal intermittency in pulsatile pipe flow. Entropy 2021;23:46.
[72] Bosch E, van de Water W. Spatiotemporal intermittency in the Faraday experiment. Phys Rev Lett 1993;70:3420.
[73] Yasuda T, Vassilicos JC. Spatio-temporal intermittency of the turbulent energy cascade. J Fluid Mech 2018;853:235.
[74] Chaté H. Spatiotemporal intermittency regimes of the one-dimensional complex Ginzburg–Landau equation. Nonlinearity 1994;7:185.
[75] Chaté H, Manneville P. Spatiotemporal intermittency turbulence: a tentative dictionary, vol. 341, N.Y: Plenum Press; 1995, p. 111–6,
[76] Snouck D, Westra M-T, van de Watera W. Turbulent parametric surface waves. Phys Fluids 2009;21:025102.
[77] Julius S, Garih H, Estivalezes JL, Casalis G. Vibration-induced instability of a fluid film flowing down a vertical plane: Experimental and numerical comparison. Phys Fluids 2019;31:104111.
[78] Kudrolli A, Gollub JE. Patterns and spatiotemporal chaos in parametrically forced surface waves: a systematic survey at large aspect ratio. Phys D 1996;97:133.
[79] Gluckman BJ, Marcq P, Bridger J, Gollub JP. Time averaging of chaotic spatiotemporal wave patterns. Phys Rev Lett 1993;71:2034.
[80] Lioubashevski O, Fineberg J, Tuckerman LS. Scaling of the transition to parametrically driven surface waves in highly dissipative systems. Phys Rev E 1997;55. R3832(R).
[81] Zhang W, Viñals J. Secondary instabilities and spatiotemporal chaos in parametric surface waves. Phys Rev Lett 1995;74:690.
[82] Alvarez-Garrido F, Clerc MG, Gonzalez-Cortes G. Transition to spatiotemporal intermittency and defect turbulence in systems under translational coupling. Phys Rev Lett 2020;124:164101.
[83] Pikovsky A, Politi A. Lyapunov exponents: a tool to explore complex dynamics. Cambridge: Cambridge University Press; 2016.
[84] Kaplan JL, Yorke JA. Chaotic behavior of multidimensional difference equations. In: Peitgen HO Walther HO, editor. Functional differential equations and approximation of fixed points. Lecture notes in mathematics, vol. 730, Berlin, Heidelberg: Springer; 1979.
[85] Sulem C, Sulem PL. The nonlinear Schrödinger equation: Self-focusing and wave collapse. Springer-Verlag; 1999.
[86] Pétrélis F, Aumaître S, Fauve S. Phys Rev Lett 2005;94:070603.
[87] Kernighan BW, Ritchie DM. The C programming language. 2nd ed. New Jersey: Prentice Hall; 1988.
[88] https://www.gnu.org/software/gsl/.
[89] https://numpy.org.
[90] Wolf A, Swift JB, Swinney HL, Vastano JA. Determining Lyapunov exponents from a time series. Phys D 1985;16:285.
[91] Karimi A, Paul MR. Extensive chaos in the Lorenz-96 model. Chaos 2010;20:043105.
[92] Eckmann JP, Ruelle D, Ciliberto S. Liapunov exponents from time series. Phys Rev A 1986;34:4971.
[93] Geist K, Parlitz U, Lauterborn W. Comparison of different methods for computing Lyapunov exponents. Progr Theoret Phys 1990;83:875.
[94] Sprott JC. Chaos and time-series analysis. UK: Oxford University Press; 2003.
[95] Scheel JD, Cross MC. Lyapunov exponents for small aspect ratio Rayleigh-Bénard convection. Phys Rev E 2006;74:066301.
[96] Karimi A, Paul MR. Quantifying spatiotemporal chaos in Rayleigh-Bénard convection. Phys Rev E 2012;85:046201.
[97] Gallas JAC. The structure of infinite periodic and chaotic hub cascades in phase diagrams of simple autonomous flows. Int J Bifurcation Chaos 2010;20:197.
[98] Laroze D, Bragard J, Suarez OJ, Pleiner H. Characterization of the chaotic magnetic particle dynamics. IEEE Trans Magn 2011;47:3032.
[99] Bragard J, Pleiner H, Suarez OJ, Vargas P, Gallas JAC, Laroze D. Chaotic dynamics of a magnetic nanoparticle. Phys Rev E 2011;84:037202.
[100] Laroze D, Becerra-Alonso D, Gallas JAC, Pleiner H. Magnetization dynamics under a quasiperiodic magnetic field. IEEE Trans Magn 2012;48:3567.
[101] Brugnago EL, Gallas JAC, Beims MW. Predicting regime changes and durations in Lorenz's atmospheric convection model. Chaos 2020;30:083106.
[102] Clerc MG, Verschueren N. Quasiperiodicity route to spatiotemporal chaos in one-dimensional pattern-forming systems. Phys Rev E 2013;88:052916.
[103] Bonatto C, Gallas JAC. Periodicity hub and nested spirals in the phase diagram of a simple resistive circuit. Phys Rev Lett 2008;101:054101.
[104] Ramirez-Avila GM, Gallas JAC. How similar is the performance of the cubic and the piecewise-linear circuits of chua? Phys Lett A 2010;375:143.
[105] Vélez JA, Bragard J, Pérez LM, Cabanas AM, Suarez OJ, Laroze D, Mancini HL. Periodicity characterization of the nonlinear magnetization dynamics. Chaos 2020;30:093112.
[106] Mahmud MN, Siri Z, Vélez JA, Pérez LM, Laroze D. Chaotic convection in an Oldroyd viscoelastic fluid in saturated porous medium with feedback control. Chaos 2020;30:073109.
[107] Laroze D, Pleiner H. Thermal convection in a nonlinear non-Newtonian magnetic fluid. Commun Nonlinear Sci Numer Simul 2015;26:167.
[108] Laroze D, Siddheshwar PG, Pleiner H. Chaotic convection in a ferrofluid. Commun Nonlinear Sci Numer Simul 2013;18:2436.
[109] Siddheshwar PG, Kanchana C, Laroze D. A study of Darcy-Benard regular and chaotic convection using a new local thermal non-equilibrium formulation. Phys Fluids 2021;33:044107.
[110] Kanchana C, Vélez JA, Pérez LM, Laroze D, Siddheshwar PG. Influence of higher-order modes on ferroconvection. Chaos 2022;32:083129.
[111] Pérez LM, Vélez JA, Mahmud MN, Corona RM, Castillo-Sepúlveda S, Pedraja-Rejas L, et al. Complexity measurements for the thermal convection in a viscoelastic fluid saturated porous medium. Results Phys 2023;52:106737.
[112] Liu Z, Ouali M, Coulibaly S, Clerc MG, Taki M, Tlidi M. Characterization of spatiotemporal chaos in a Kerr optical frequency comb and in all fiber cavities. Opt Lett 2017;42(6):1063.
[113] Ferré MA, Clerc MG, Coulibally S, Rojas RG, Tlidi M. Localized structures and spatiotemporal chaos: comparison between the driven damped sine-Gordon and the Lugiato–Lefever model. Eur Phys J D 2017;71:172.
[114] Panajotov K, Clerc MG, Tlidi M. Spatiotemporal chaos and two-dimensional dissipative rogue waves in Lugiato–Lefever model. Eur Phys J D 2017;71:176.